Numerical Experiments in Synthetic Jet Based Separation Control

Rupesh B. Kotapati * and Rajat Mittal †

Department of Mechanical and Aerospace Engineering

The George Washington University, Washington, DC, 20052, USA

Louis N. Cattafesta III ‡

Department of Mechanical and Aerospace Engineering

University of Florida, Gainesville, FL, 32611, USA

Two-dimensional numerical simulations have been carried out in a flow configuration devised for investigating synthetic jet based active separation control. The numerical configuration consists of a 2% thick elliptic plate at zero incidence in a free-stream. A separation bubble of prescribed size is created on the top surface of the plate at a desired location by applying blowing and suction on the top boundary of the computational domain. This flow is characterized by three distinct time scales corresponding to the shear layer, the separation zone and the vortex shedding in the wake and can therefore be considered a canonical separated airfoil flow. Simulations of this flow at a chord Reynolds number of $60,000$ subject to zero-net-mass-flux (ZNMF) perturbation of the boundary layer at different characteristic time-scales are presented. Results from the computations indicate that ZNMF forcing at a frequency corresponding to the separation zone or its subharmonic draws a better response as compared to excitation at the shear layer frequency or its super-harmonic. Results also show that locating the ZNMF device upstream of the separation bubble leads to a more effective separation control than when the ZNMF device is located inside the separation bubble.

Nomenclature

f_J	Forcing frequency of the ZNMF device, Hz.
f_{sep}	Separation bubble frequency, Hz.
f_{SL}	Shear layer frequency, Hz.
f_{wake}	Wake vortex shedding frequency, Hz.
H_{sep}	Height of the separation bubble, m.
L_{sep}	Length of the separation bubble, m.
Re	Reynolds number based on free-stream velocity and chord length, $Re = U_\infty c/\nu$.
U_∞	Free-stream velocity, m/s.
$V_J(t)$	Oscillatory exit velocity of the ZNMF device, m/s.
c	Airfoil chord, m.

*Doctoral Candidate & Presidential Fellow; rupesh@gwu.edu, Student Member AIAA.

†Associate Professor; mittal@gwu.edu, Associate Fellow AIAA.

‡Associate Professor; cattafes@ufl.edu, Associate Fellow AIAA.

p Pressure, N/m^2.
t Time, s.
u, v Streamwise and cross-stream velocity components, respectively, m/s.
u_i General notation for velocity components; $u_1 \equiv u$, $u_2 \equiv v$.
u_i' Fluctuating velocities, m/s.
x_i General notation for spatial coordinates; $x_1 \equiv x$, $x_2 \equiv y$.
x_J Streamwise location of ZNMF forcing, m.
x_{sep} Streamwise location of separation, m.
X_{TE} Distance between the separation location and the trailing edge.

Subscripts

i Directional index, $i = 1, 2$.

Symbols

ν Kinematic viscosity, m^2/s.
ω_z Instantaneous spanwise vorticity, 1/s.
ρ Density, kg/m^3.

I. Introduction

DESPITE extensive prior research in active separation control, numerous unresolved technical issues remain concerning the different strategies, mechanisms, and scaling laws for successful control of separation using zero-net mass-flux (ZNMF) actuators. Experimental investigations[1,2] have shown that accelerated transition of a laminar boundary layer to turbulence does not play a pivotal role in ZNMF based separation control. A fundamental mechanism that is identified in ZNMF based active separation control is the formation of large-scale vortices in the separated shear layer due to oscillatory forcing, which entrain outer high-momentum fluid into the boundary layer, thereby delaying separation or even reattaching a separated flow. Control schemes that harness this mechanism are usually based on a sequence of propositions and Mittal *et al.*[3,4] have critically evaluated each of these propositions in order to highlight the sources of ambiguity and provide guidance for further research.

Key issues that require systematic study are optimal excitation frequencies and waveforms, pressure gradient, and curvature effects in separated flows characterized by convective and/or global instabilities. Here, the optimality is defined with respect to the condition of maximal flow attachment as measured by the mean surface shear stress. Past approaches to studying these issues have mostly employed conventional airfoil geometries where the flow separation is produced by varying angle-of-attack and/or free-stream velocity. Although this approach is obviously grounded in practical reality, it is not amenable for a precise investigation and delineation of the various physical mechanisms that are potentially implicated in active separation control. For instance, consider flow over an airfoil at incidence where separation occurs at some location downstream of the leading edge, and the separated shear layer may or may not reattach before the trailing edge. If the flow reattaches before the trailing edge, there are potentially three distinct frequency scales: f_{SL}, the frequency of the roll-up of the shear layer; f_{sep}, the frequency scale corresponding to the separation bubble; and f_{wake}, the wake shedding frequency.

For a shear layer that separates from and reattaches to a solid surface, the presence of a near-wall reversed flow region permits upstream propagation of disturbances and alters the stability characteristics of the shear layer. In this case, the frequency corresponding to the separation region scales as $f_{sep} \sim U_\infty / L_{sep}$. The wake shedding frequency, however, is active for all cases and due to its global effect, probably plays some role in the dynamics of the flow. The scaling for Kármán vortex shedding due to Roshko[5] is $f_{wake} \sim U_\infty / W_{wake}$, which is fundamentally different from that of f_{sep}. For a shear layer that separates and does not reattach, the shear layer instability frequency f_{SL} plays an important role. This frequency scales more like that of a free shear layer (see Ho & Huerre[6]), i.e. $f_{SL} \sim \bar{U}/\theta$, where $\bar{U}$ is the average velocity across the shear

layer, and θ is the momentum thickness. In order to examine the scaling of these frequencies as well as their potential nonlinear interactions, it would be extremely useful to separately prescribe the extent and location of the separation bubble as well as the Reynolds number.

In this study, a novel numerical configuration has been devised for investigating active control of separated airfoil flows. Previously, two-dimensional simulations of this configuration without separation control by Mittal *et al.*[3,4] have shown that these canonical separated airfoil flows are indeed characterized by three distinct time scales corresponding to the shear layer, the separation zone, and the vortex shedding in the wake. The resonant interaction between these different scales is dependent on the distance between the separation location and the trailing edge (X_{TE}) as well as the chord-wise location of separation (x_{sep}). Two-dimensional simulations of a canonical separated airfoil flow at a Reynolds number of $60,000$ subjected to zero-net-mass-flux (ZNMF) perturbation of the boundary layer are presented. The key control parameters in a ZNMF device are the jet frequency f_J and the characteristic jet velocity V_J. Since the control authority varies monotonically with V_J (Seifert *et al.*,[1,7,8] Glezer & Amitay,[9] Mittal & Rampunggoon[10]) up to a point where a further increase would lead to complete disruption of the boundary layer, there is a little leeway for optimizing the ZNMF device with respect to V_J. On the other hand, the control authority has a highly non-monotonic variation with f_J (Seifert & Pack,[11] Greenblatt & Wygnanski,[12] Glezer *et al.*[2]) and offers the potential for optimizing f_J. Also, Pack *et al.*[13] have found that low frequency amplitude modulation (AM) of the high resonant frequency of a ZNMF device required approximately 50% less momentum input to achieve the same performance gains. Therefore, two-dimensional simulations are carried out with ZNMF perturbation of the boundary layer with various frequencies and duty cycles with a fixed jet velocity V_J. The simulations allow us to assess the effect of these variations on the control authority.

II. Flow Configuration

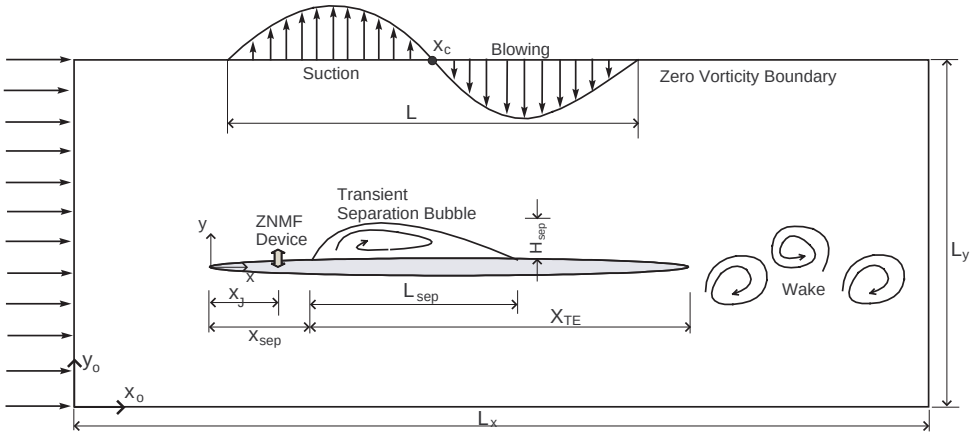

Figure 1. Schematic of the flow configuration (not to scale).

The configuration considered in the present study consists of an elliptic airfoil with chord c and thickness $t = 0.02c$ at zero degrees angle-of-attack in a free-stream. The schematic is shown in figure 1. The origin of the global coordinate system (x_o, y_o) is fixed at the lower left-hand corner of the computational domain that measures L_x and L_y in x_o and y_o directions, and the origin of the local coordinate system (x, y) is at the leading edge of the airfoil. A separation bubble of prescribed size is induced at a desired location on the upper surface of the airfoil by applying an adverse pressure gradient through blowing and suction on the upper boundary of the computational domain. Following Na & Moin,[14] we prescribe a zero-vorticity

boundary condition of the following form on the upper boundary:

$$v(x_o, L_y) = G(x_o), \qquad \left.\frac{\partial u}{\partial y_o}\right|_{(x_o, L_y)} = \frac{dG}{dx_o}, \tag{1}$$

where $G(x_o)$ is the prescribed blowing and suction velocity profile, and the Neumann boundary condition on u ensures that no spanwise vorticity (ω_z) is generated due to blowing and suction. The function $G(x_o)$ allows us to prescribe the location as well as the streamwise size of the separation region. In this study, $G(x_o)$ is of the form:

$$G(x_o) = -V_{top} sin\left(\frac{2\pi(x_o - x_c)}{L}\right) e^{-\alpha\left(\frac{2(x_o - x_c)}{L}\right)^{\beta}}, \tag{2}$$

where x_c is the center of the blowing and suction velocity profile in the global system and L is the length of the profile (see figure 1 on the page before). The parameters V_{top}, α and β are set to $0.8U_\infty$, 10 and 20, respectively. It should be noted that the lower boundary is also assumed to be a zero-vorticity wall with no blowing or suction. This configuration serves the following purposes: (1) It is simple and includes all the features of a canonical separated flow such as the leading edge boundary layer inception, open/closed suction side separation and a wake that includes vortices from the suction and pressure sides; (2) It allows for independent prescription of the location and size of the separation region as well as the Reynolds number; and (3) It permits independent prescription of the adverse pressure gradient without the confounding effect of curvature. The above configuration helps us to examine the nonlinear interactions between the shear layer, separation region and airfoil wake, with or without separation control, in the absence of the effects of curvature.

All simulations reported in the current study are carried out at a Reynolds number Re (based on the free-stream velocity and chord length) of $60,000$ on a Cartesian grid with 640×220 mesh points. Mid-chord separation is induced on the upper surface of the airfoil by prescribing blowing and suction over $0.25 \leq x/c \leq 0.75$ on the top boundary of the computational domain. The bubble is closed prior to the trailing edge in an attempt to decouple the global instability of the wake from the local instabilities of the separated shear layer and the separation zone. First, the uncontrolled version of this flow configuration with mid-chord separation is simulated to determine the three different frequency-scales: f_{SL}, the frequency of the roll-up of the shear layer; f_{sep}, the frequency scale corresponding to the separation bubble; and f_{wake}, the wake shedding frequency. After determining these different frequency-scales, simulations are carried out with ZNMF perturbation of the boundary layer at various frequencies detailed in table 1. The effect of the ZNMF device is modeled by prescribing a localized oscillatory normal velocity of the form $V_J(t) = V_0 sin(2\pi f_J t)$ with $V_0 = 0.1U_\infty$ over a length of $0.01c$ on the upper surface of the airfoil. Two streamwise locations are considered in the present study for ZNMF forcing – one just upstream of the separation location and the other at the center of the separation bubble. A case of amplitude modulation that uses a forcing of the form $V_J(t) = V_0 sin(2\pi f_{AM} t) sin(2\pi f_c t)$, where $f_{AM} << f_c$, is also considered with $V_0 = 0.1U_\infty$, $f_c = 2f_{SL}$, and $f_{AM} = f_{sep}$.

III. Numerical Methodology

The flow field is modeled by two-dimensional unsteady incompressible Navier-Stokes equations in primitive variables (velocity and pressure), written in tensor form as

$$\frac{\partial u_i}{\partial x_i} = 0 \tag{3}$$

$$\frac{\partial u_i}{\partial t} + \frac{\partial u_i u_j}{\partial x_j} = -\frac{1}{\rho}\frac{\partial p}{\partial x_i} + \nu \frac{\partial^2 u_i}{\partial x_j \partial x_j} \tag{4}$$

Table 1. Various cases considered in the present study, $Re = 60,000$, $V_0/U_\infty = 0.1$.

Case	Forcing frequency f_J	ZNMF location x_J/c
1	No forcing	–
2	$f_{sep}/2 = 1.75U_\infty/c$	0.2
3	$f_{sep} = 3.5U_\infty/c$	0.2
4	$f_{SL} = 2f_{sep} = 7.0U_\infty/c$	0.2
5	$2f_{SL} = 14.0U_\infty/c$	0.2
6	$f_c \pm f_{AM} = 2f_{SL} \pm f_{sep} = (14.0 \pm 3.5)U_\infty/c$	0.2
7	$f_{sep} = 3.5U_\infty/c$	0.4

where the indices, $i = 1, 2$, represent the x and y directions, respectively, t is the time, ν is the kinematic viscosity, p is the pressure and the components of the velocity vector $\boldsymbol{u}$ are denoted by u and v. The equations are non-dimensionalized with the chord length c and free-stream velocity U_∞, and discretized using a cell-centered, collocated (non-staggered) arrangement of the primitive variables $(\boldsymbol{u}, p)$. In addition to the cell-center velocities $(\boldsymbol{u})$, the face-center velocities $(\boldsymbol{U})$, are also computed. Similar to a fully staggered arrangement, only the component normal to the cell-face is calculated and stored. The face-center velocity is used for computing the volume flux from each cell. The advantage of separately computing the face-center velocities is discussed in the context of the current method in Ye *et al.*.[15] The equations are integrated in time using a two-step second-order accurate fractional step method. In the first step, the momentum equations without the pressure gradient terms are advanced in time. In the second step, the pressure field is computed by solving a Poisson equation. A second-order Adams-Bashforth scheme is employed for the convective terms while the diffusion terms are discretized using an implicit Crank-Nicolson scheme which eliminates the viscous stability constraint. The pressure Poisson equation is solved with an efficient multi-grid method.

A multi-dimensional ghost-cell methodology (GCM) is used to incorporate the effect of the immersed boundary on the flow. The general framework can be considered as Eulerian-Lagrangian, wherein the immersed boundaries are explicitly tracked as surfaces in a Lagrangian mode, while flow computations are performed on a fixed Eulerian mesh. Hence, grid cells that are just inside the immersed boundaries are tagged as "ghost cells" as opposed to regular "fluid cells". The discrete equations for these cells are then formulated so as to satisfy the imposed boundary condition on the nearby flow boundary to second-order accuracy. These equations are then solved in a fully coupled manner with the governing flow equations of the regular fluid cells. Care has been taken to ensure that the discretized equations for the ghost cells satisfy local and global mass conservation constraints as well as pressure-velocity compatibility relations. The reader is referred to the work of Bozkurttas *et al.*[16] for detailed implementation of the ghost-cell method. The numerical method and the associated flow solver have been validated in several flows by comparisons against established experimental and computational data. Details have been presented elsewhere.[17]

IV. Results and Discussion

Figure 2 on the following page that shows the contour plot of spanwise vorticity $(\omega_z c/U_\infty)$ for Case 1 clearly delineates the distinct features present in the flow field. The boundary layer on the suction side loses momentum due to adverse pressure gradient induced by blowing and suction on the top boundary, separates at the location where the suction becomes active and starts rolling up into Kelvin-Helmholtz (KH) type vortices. These small scale vortical structures coalesce and form larger vortices in the separated region. When these large vortices are of some appropriate size, they are periodically released from the separation zone and travel downstream to disrupt the Kármán vortex shedding in the wake. The plot of

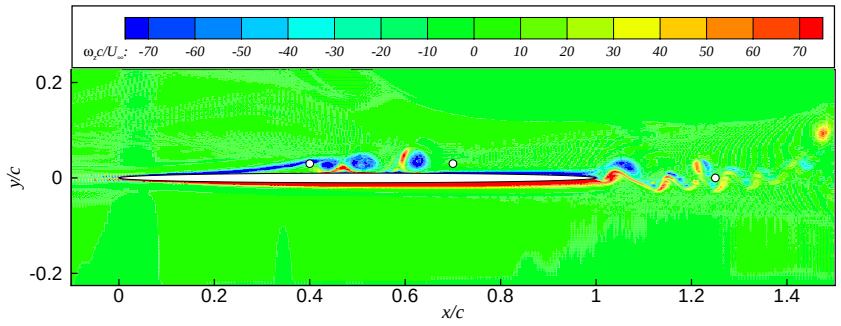

Figure 2. Contour plot of instantaneous spanwise vorticity ($\omega_z c/U_\infty$) for Case 1. The plot also shows "probe" locations where the time series of cross-stream velocity is recorded for spectral analyses.

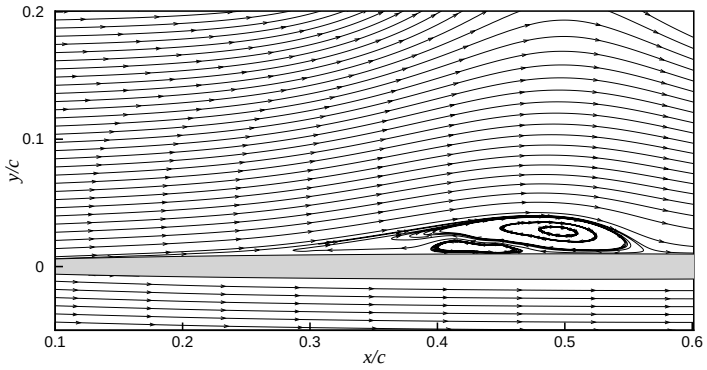

Figure 3. Streamlines corresponding to time-averaged velocity field for Case 1.

streamlines for Case 1 in figure 3 shows the separation bubble corresponding to time-averaged velocity field. The separation occurs at $x_{sep} = 0.239c$ from the leading edge and the streamwise length (L_{sep}) and height (H_{sep}) of the separation bubble are estimated to be $0.331c$ and $0.03c$, respectively. Figure 4 on the following page shows the temporal variations of the cross-stream velocity component v/U_∞ and their corresponding power spectra E_v for the baseline uncontrolled flow (Case 1) at three stations $x/c = 0.4$, 0.7 and 1.25 that correspond to locations of shear layer roll-up, expulsion of large vortices from the separation zone, and vortex shedding in the wake, respectively. The spectra are obtained by computing fast Fourier transforms (FFT) of the cross-stream velocity component recorded over ten convective time scales. Temporal variation at $x/c = 0.4$ shows the presence of high frequency content corresponding to the roll-up of the shear layer into Kelvin-Helmholtz (KH) type vortices, and the corresponding power spectrum shows that $f_{SL}c/U_\infty \approx 7$. The temporal variation at $x/c = 0.7$ indicates the presence of low separation bubble frequency corresponding to the periodic release of vortical structures from the separation zone. The corresponding frequency spectrum indicates that the separation bubble frequency $f_{sep}c/U_\infty \approx 3.5$. Thus, the separation bubble frequency manifests as a subharmonic of the shear layer frequency due to the coalescence of the Kelvin-Helmholtz type vortices generated from the roll-up of the shear layer. Temporal variation of the cross-stream velocity in the wake also shows periodic disruption of the high frequency vortex shedding by the vortices released from the separation zone and the corresponding wake frequency $f_{wake}c/U_\infty$ is estimated from the spectrum to be 12.5. As expected, the second peak in the power spectrum of the wake corresponds to the same value of the separation bubble frequency as estimated from the spectrum in the region downstream of the separation zone.

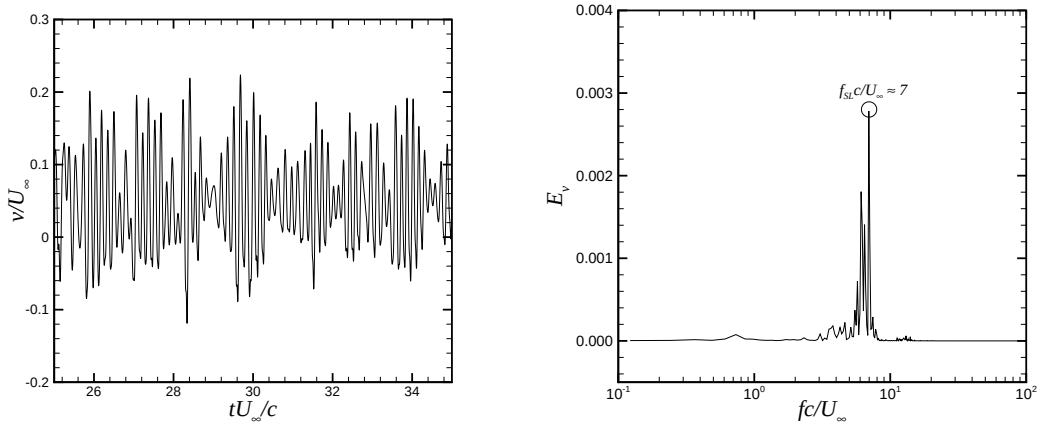

(a) $x/c = 0.40,\ y/c = 0.03$

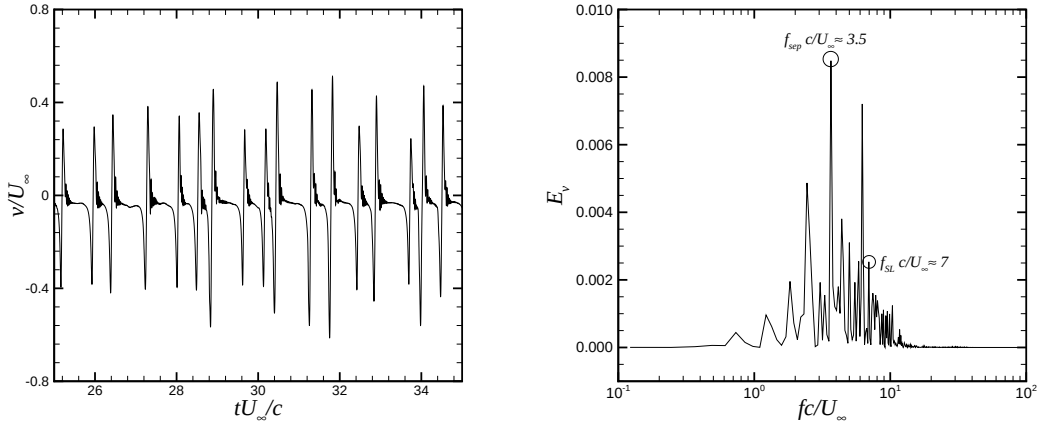

(b) $x/c = 0.70,\ y/c = 0.03$

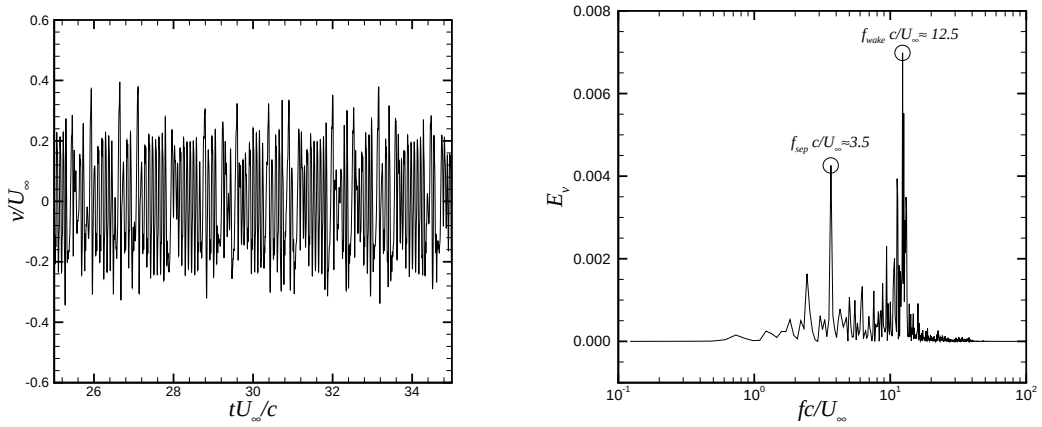

(c) $x/c = 1.25,\ y/c = 0.0$

Figure 4. Temporal variations of the cross-stream velocity (left) and their corresponding frequency spectra (right) at various locations for Case 1. Locations of these "probe" points are shown in figure 2.

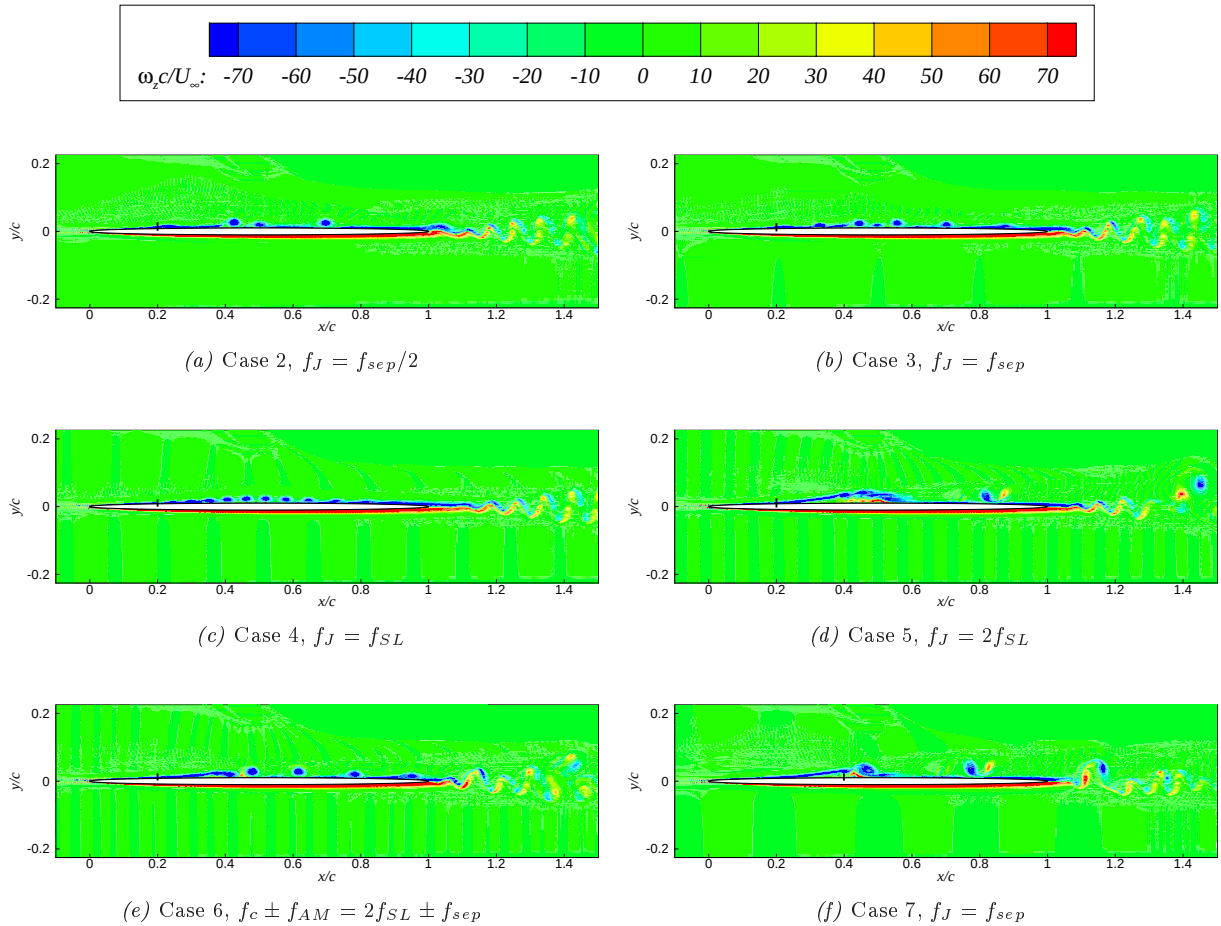

(a) Case 2, $f_J = f_{sep}/2$

(b) Case 3, $f_J = f_{sep}$

(c) Case 4, $f_J = f_{SL}$

(d) Case 5, $f_J = 2f_{SL}$

(e) Case 6, $f_c \pm f_{AM} = 2f_{SL} \pm f_{sep}$

(f) Case 7, $f_J = f_{sep}$

Figure 5. Contour plots of instantaneous spanwise vorticity ($\omega_z c/U_\infty$) for various cases. The location of ZNMF forcing is shown by a "post" on the suction side.

The baseline uncontrolled flow in Case 1 is subject to ZNMF forcing from $t = 25c/U_\infty$ at various frequencies detailed in table 1. Figures 5(a) through 5(f) show contours of spanwise vorticity ($\omega_z c/U_\infty$) for cases 2 through 7, respectively. Since $f_{SL} \approx 2f_{sep}$, Case 4 can be regarded as corresponding to ZNMF perturbation at either f_{SL} or $2f_{sep}$. It is evident from the contours of spanwise vorticity that ZNMF forcing at low frequencies (cases 2, 3 and 4) yields a positive response with the separated shear layer reattaching to the airfoil surface over a significant portion of the chord. This is also evident from the plot of streamlines corresponding to the time-averaged velocity field for cases 2–4 shown in figures 6(a) through 6(c). While separation is completely suppressed in the mean flow for cases 2 and 3, a very shallow separation bubble is seen for Case 4. It will be shown later using spectral analyses that for ZNMF forcing at $f_J c/U_\infty = 1.75$, 3.5, and 7.0, the shear layer and the separation zone lock-on to the forcing frequency through resonance. However, on the other hand, as shown in the contour plot of instantaneous vorticity for Case 5 (figure 5d), ZNMF forcing at a high frequency close to the wake frequency or twice the shear layer frequency has very little or no effect on the separation process. Also, the separation bubble portrayed by mean flow streamlines for this case (figure 6d) is of the same size as the separation bubble in the uncontrolled flow. This can be attributed to the fact that the high perturbation frequency does not couple significantly with either the separation bubble or the shear layer frequency.

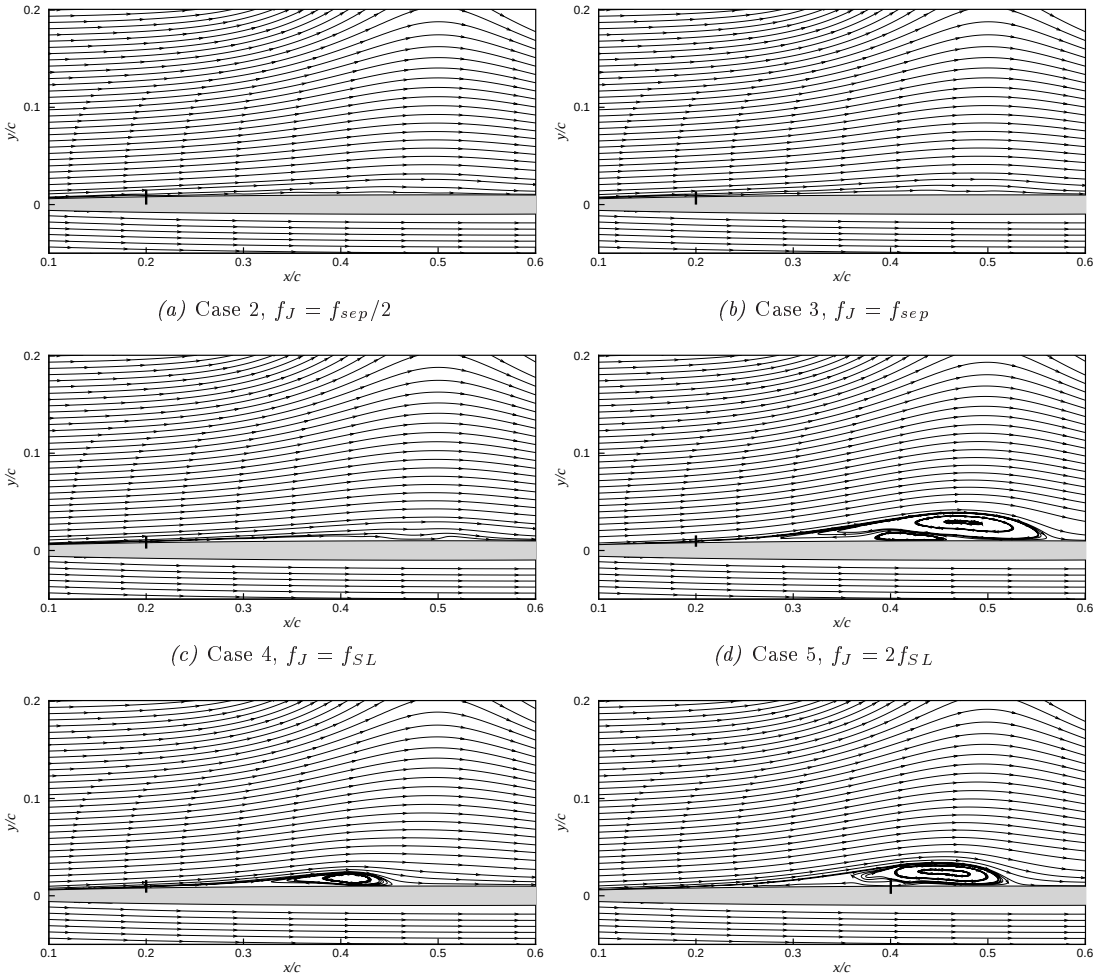

(a) Case 2, $f_J = f_{sep}/2$

(b) Case 3, $f_J = f_{sep}$

(c) Case 4, $f_J = f_{SL}$

(d) Case 5, $f_J = 2f_{SL}$

(e) Case 6, $f_c \pm f_{AM} = 2f_{SL} \pm f_{sep}$

(f) Case 7, $f_J = f_{sep}$

Figure 6. Streamlines corresponding to time-averaged velocity field for various cases.

ZNMF forcing using amplitude modulation of twice the shear layer frequency ($2f_{SL}$) by the separation bubble frequency (f_{sep}) delays the separation of the shear layer and leads to a smaller separation bubble than that formed in the uncontrolled flow. Contours of instantaneous spanwise vorticity ($\omega_z c/U_\infty$) and plot of streamlines for this case (Case 6) are shown in figures 5(e) and 6(e), respectively. In order to study the effect of streamwise location (x_J) of ZNMF perturbation on separation control, the ZNMF forcing at separation bubble frequency f_{sep} is repeated at $x_J = 0.4c$ in Case 7. The station $x_J = 0.4c$ approximately corresponds to the center of the time-averaged separation bubble obtained for Case 1. Contours of instantaneous spanwise vorticity and plot of streamlines shown for this case in figures 5(f) and 6(f), respectively, indicate that the ZNMF perturbation inside the separation zone only results in a small reduction in the height of the time-averaged separation bubble. The location of separation (x_{sep}), and the length (L_{sep}) and the height (H_{sep}) of the separation bubble for various cases are summarized in table 2 on the next page.

Figures 7(a) through 7(f) show the power spectra corresponding to the temporal variation of the cross-stream velocity in the shear layer for cases 2 through 7, respectively. The spectra for cases 2, 3, 4 and 7

Table 2. Location and size of the separation bubble for various cases.

Case	x_{sep}	L_{sep}	H_{sep}
1	0.239c	0.331c	0.030c
2	–	–	–
3	–	–	–
4	0.264c	0.156c	0.005c
5	0.236c	0.337c	0.031c
6	0.245c	0.213c	0.014c
7	0.239c	0.293c	0.024c

indicate that the shear layer is able to respond to forcing at low frequencies, thereby allowing it to lock-on to the forcing frequency or its super-harmonic, regardless of whether the ZNMF forcing is located upstream of or within the separation bubble. It is clear from the power spectrum for Case 5 shown in figure 7(d) that the high forcing frequency does not couple with the frequency of the shear layer. Also, for the case of amplitude modulation of high frequency ($2f_{SL}$) with the low frequency of the separation zone (f_{sep}) shown in figure 7(e), nonlinear dynamics of the flow causes the low frequency to result and force the flow. Similar power spectra in the region downstream of the separation zone are shown in figures 8(a) through 8(f). Similar to the spectra in the shear layer, the spectra in the region downstream of the separation zone indicate that for ZNMF forcing at low frequencies upstream of the separation point (cases 2, 3 and 4), the separation zone is able to lock-on to the forcing frequency or its super-harmonics, whereas at high forcing frequency (Case 5), the separation zone does not couple with the ZNMF forcing. For Case 6, figure 8(e) shows that the low modulation frequency ($f_{AM} = f_{sep}$) dominates over the high carrier frequency ($f_c = 2f_{SL}$) and forces the separation zone. For Case 7 with the ZNMF forcing inside the separation bubble, figure 8(f) indicates that the dominant frequency of the separation zone does not resonate with the forcing frequency.

Now, we focus our attention on the effect of ZNMF forcing on the vortex shedding in the wake. Figures 9(a) through 9(f) show the power spectra corresponding to the temporal variation of cross-stream velocity in the wake for various cases. It is clear from these plots that for cases for which ZNMF perturbation of the boundary layer eliminates or diminishes the separation bubble (cases 2, 3 and 4), the wake vortex shedding frequency $f_{wake}c/U_\infty$ is altered from its value of 12.5 in the uncontrolled case to 10.5. This is also true for the case of amplitude modulation for which it is seen from the figure 9(e) that the wake locks-on to the super-harmonic of the modulation frequency (i.e. $3f_{sep}$). On the other hand, although the high-frequency actuation shown in figure 9(d) appears to alter the dominant wake frequency, the forcing does not cause the wake to lock-on in a resonant fashion. For Case 7, the spectrum shown in figure 9(f) indicates that ZNMF forcing inside the separation zone does not change the frequency of vortex shedding in the wake. This is due to the fact that the forcing inside the separation zone is not effective in reattaching the separated flow, thereby leaving the dynamics of flow downstream of the separation bubble and in the wake mostly unchanged.

Figure 10 on page 14 shows contour plots of non-dimensional Reynolds shear stress $\langle u'v' \rangle / U_\infty^2$ for various cases considered in the present study. First, we observe that in the uncontrolled case there are two distinct regions of increased Reynolds stress, and these are associated with the separated shear layers in the separation bubble and the mixing layer in the wake. Secondly, we note that for cases 2, 3 and 4 for which ZNMF forcing is most effective, the intensity of the Reynolds stress in the otherwise separated region is lower than that obtained for cases for which forcing is not as effective. Also, the extent of the region of increased Reynolds stress in the separation zone as well as in the wake is found to be reduced for cases 2, 3 and 4 as compared to cases 5, 6 and 7.

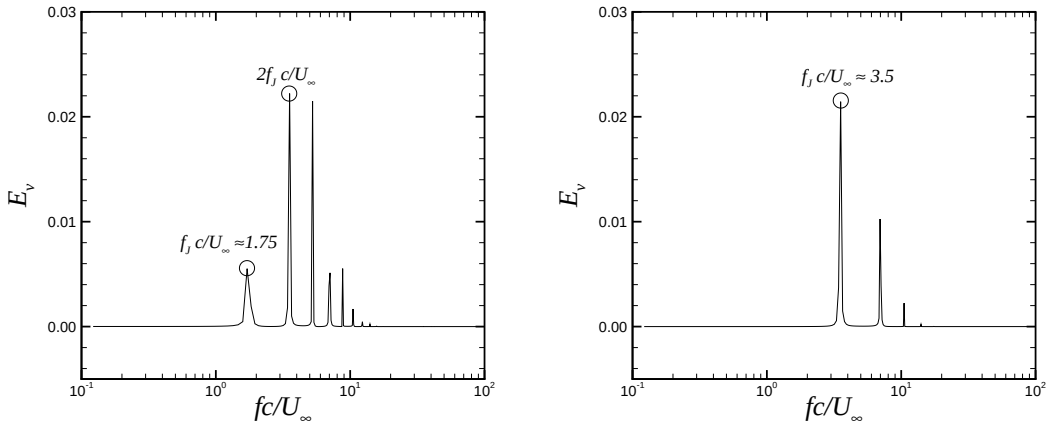

(a) Case 2, $f_J = f_{sep}/2$

(b) Case 3, $f_J = f_{sep}$

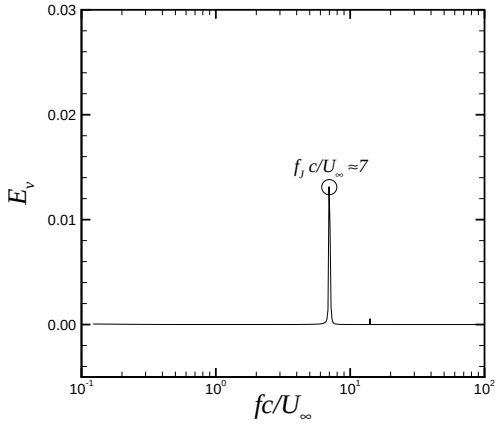

(c) Case 4, $f_J = f_{SL}$

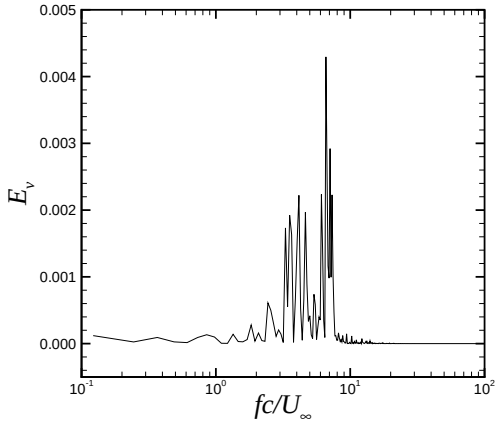

(d) Case 5, $f_J = 2f_{SL}$

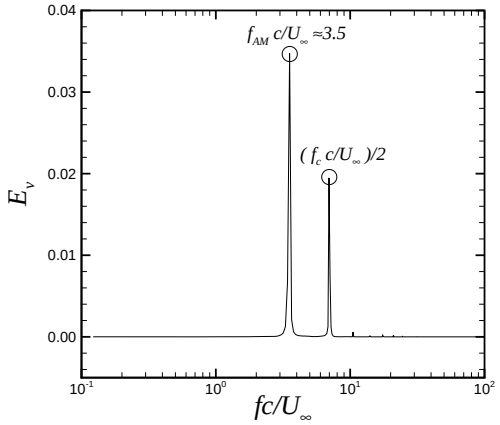

(e) Case 6, $f_c \pm f_{AM} = 2f_{SL} \pm f_{sep}$

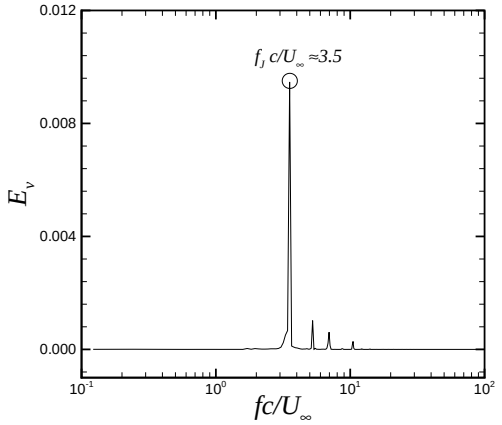

(f) Case 7, $f_J = f_{sep}$

Figure 7. Power spectra corresponding to the temporal variation of the cross-stream velocity in the shear layer at $x/c = 0.40$ and $y/c = 0.03$ for various cases.

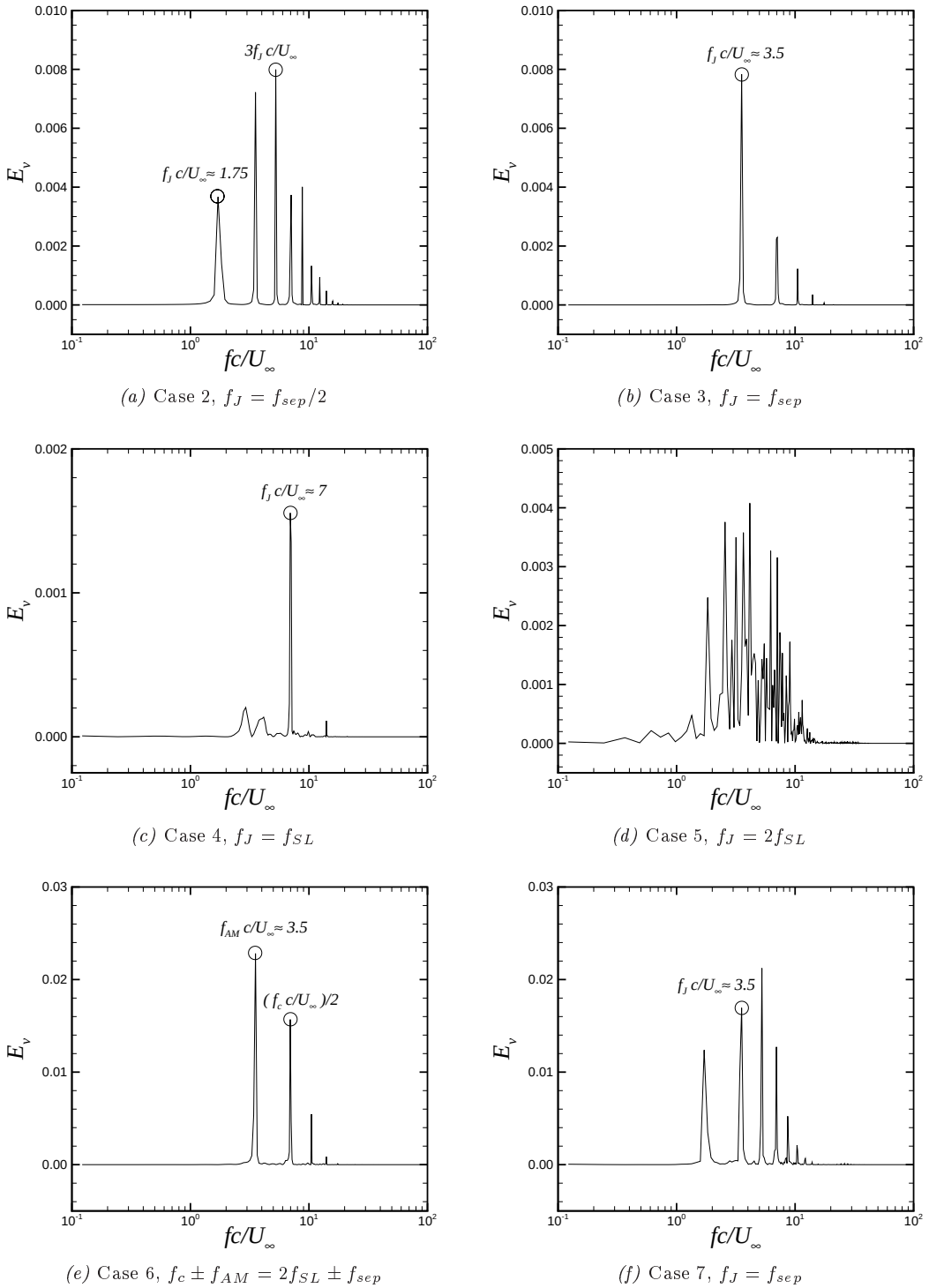

(a) Case 2, $f_J = f_{sep}/2$

(b) Case 3, $f_J = f_{sep}$

(c) Case 4, $f_J = f_{SL}$

(d) Case 5, $f_J = 2f_{SL}$

(e) Case 6, $f_c \pm f_{AM} = 2f_{SL} \pm f_{sep}$

(f) Case 7, $f_J = f_{sep}$

Figure 8. Power spectra corresponding to the temporal variation of the cross-stream velocity in the region downstream of the separation zone at $x/c = 0.70$ and $y/c = 0.03$ for various cases.

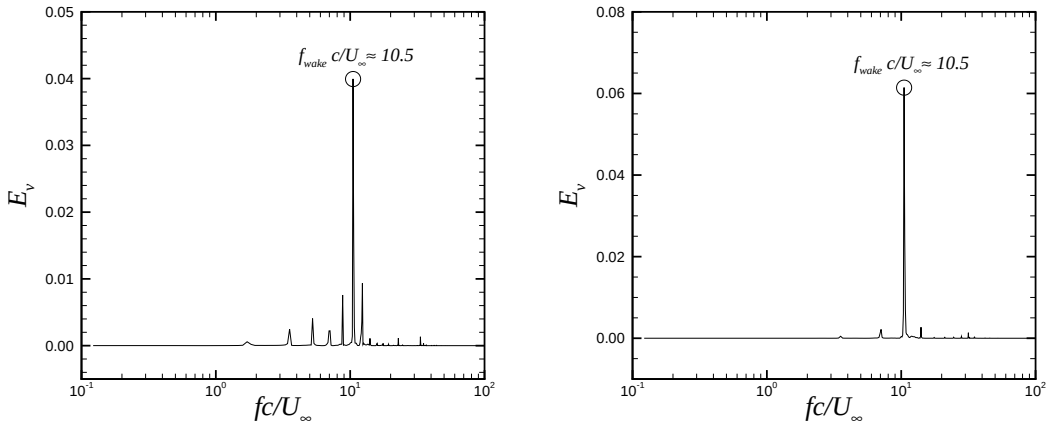

(a) Case 2, $f_J = f_{sep}/2$

(b) Case 3, $f_J = f_{sep}$

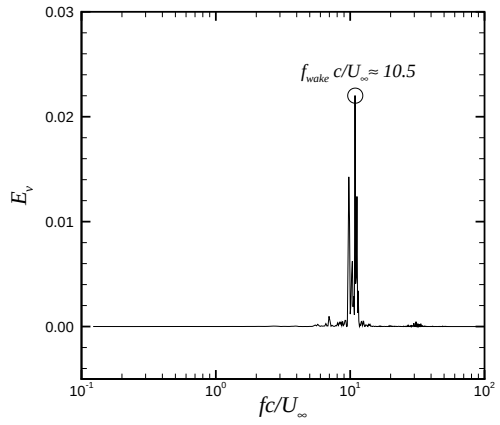

(c) Case 4, $f_J = f_{SL}$

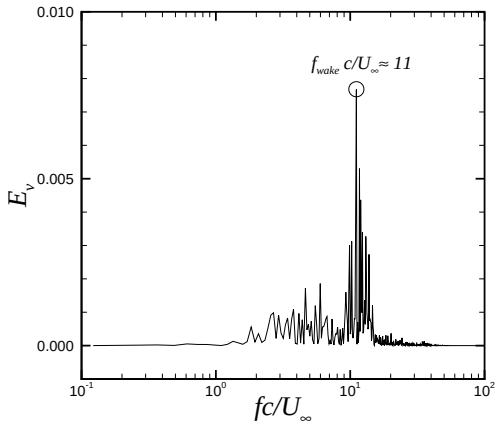

(d) Case 5, $f_J = 2f_{SL}$

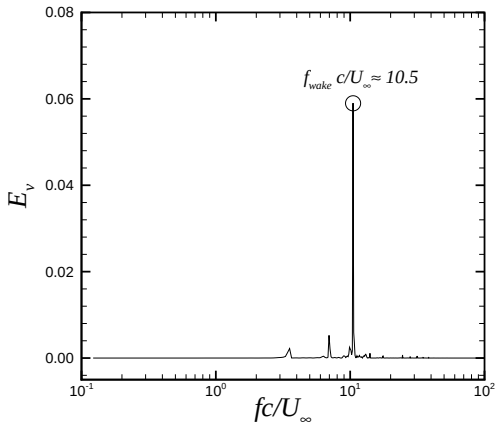

(e) Case 6, $f_c \pm f_{AM} = 2f_{SL} \pm f_{sep}$

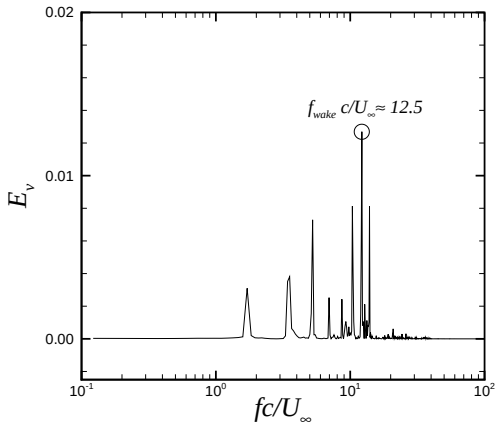

(f) Case 7, $f_J = f_{sep}$

Figure 9. Power spectra corresponding to the temporal variation of the cross-stream velocity in the wake at $x/c = 1.25$ and $y/c = 0.0$ for various cases.

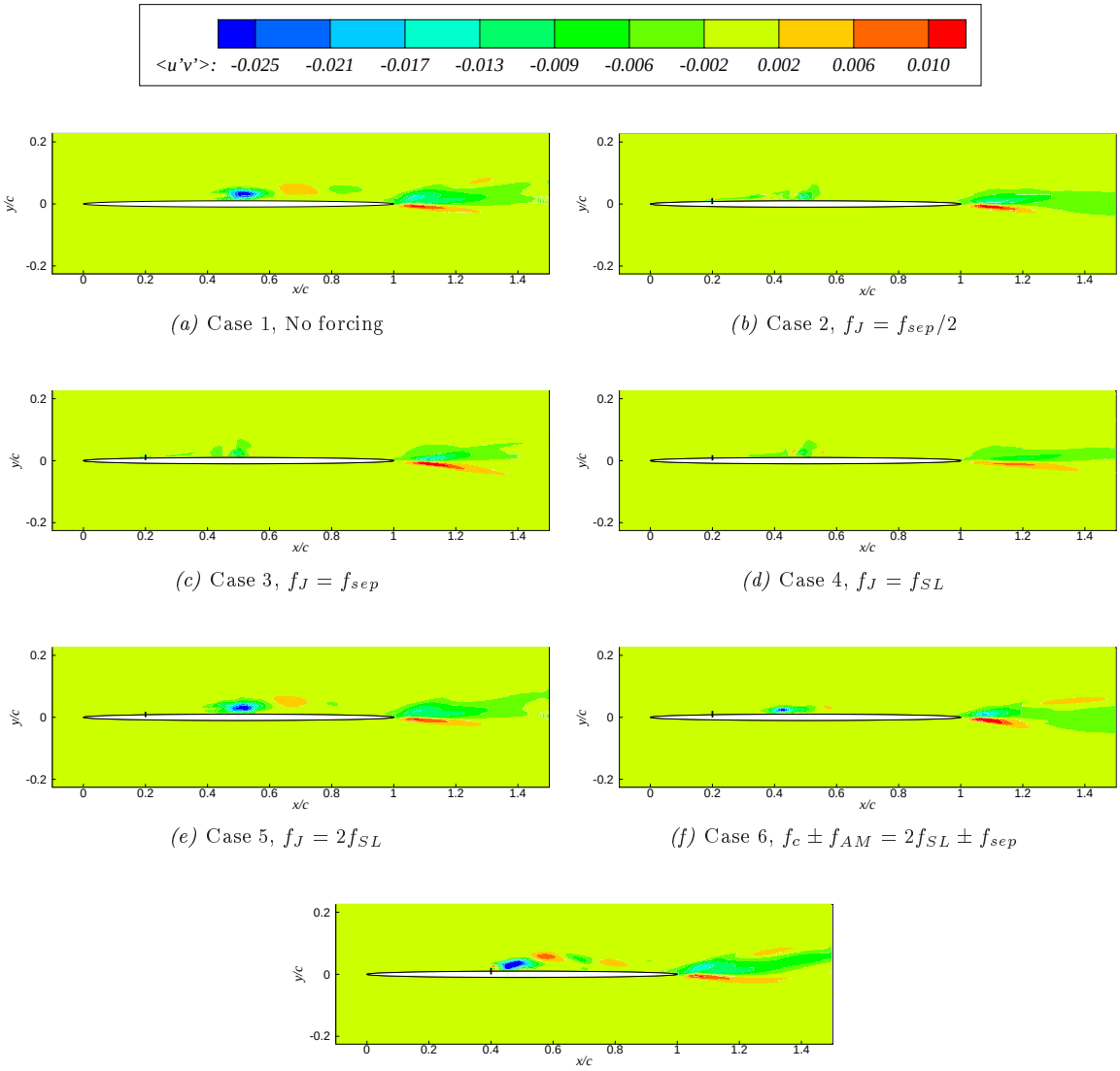

(a) Case 1, No forcing

(b) Case 2, $f_J = f_{sep}/2$

(c) Case 3, $f_J = f_{sep}$

(d) Case 4, $f_J = f_{SL}$

(e) Case 5, $f_J = 2f_{SL}$

(f) Case 6, $f_c \pm f_{AM} = 2f_{SL} \pm f_{sep}$

(g) Case 7, $f_J = f_{sep}$

Figure 10. Contour plots of non-dimensional Reynolds shear stress $\langle u'v' \rangle / U_\infty^2$ for various cases. The location of ZNMF forcing is shown by a "post" on the suction side.

V. Conclusions

Time-accurate, two-dimensional direct simulations of a novel flow configuration are used to investigate synthetic jet based separation control in a canonical separated airfoil flow. Mid-chord separation is induced on the suction side of a 2% thick elliptic flat plate at zero incidence in a free-stream by applying an adverse pressure gradient through blowing and suction on the top boundary of the computational domain. This canonical separated flow is found to be characterized by three distinct frequency scales corresponding to the shear layer, the separation region and the vortex shedding in the wake. The resulting flow at a chord Reynolds number of $60,000$ is subjected to zero-net mass-flux (ZNMF) perturbations of the boundary layer

and the response of the flow to the systematic variation of actuation frequency as well as the streamwise location of the ZNMF device is considered by focusing on the resonant interaction between the ZNMF forcing and the natural time scales of the flow. Since the point of separation is the most receptive point for a separating shear layer, it is found that forcing is most effective when applied in the vicinity of this point. On the contrary, locating the ZNMF device inside the separated region is not effective in delaying or suppressing separation. At the Reynolds number considered in the present work, spectral analyses show that at low forcing frequencies ($f_J \leq f_{SL}$) both the shear layer and the separation zone are able to lock-on to the forcing frequency or its subharmonics, whereas high actuation frequency ($f_J > f_{SL}$) does not effectively couple with the frequency of either the shear layer or the separation zone. Even though excitation at both the shear layer frequency and the separation bubble frequency (or its subharmonic) draws positive response by keeping the shear layer attached to the airfoil surface over a significant portion of the chord, actuation at the separation bubble frequency (or its subharmonic) is more effective in that it completely suppresses the mean separation bubble. Positive control of the separation zone is also found to lower the wake shedding frequency from its baseline value in the uncontrolled case.

Acknowledgments

The work presented here is supported by the U. S. Air Force Office of Scientific Research (AFOSR) under Grants F49550-05-1-0169 and FA9550-05-1-0093 monitored by Dr. Rhett Jefferies. The authors are grateful to Dr. Haibo Dong for incorporating the multi-grid method into the flow solver.

References

[1]Seifert, A., Darabi, A., and Wygnanski, I., "Delay of Airfoil Stall by Periodic Excitation," *J. Aircraft.*, Vol. 33, 1996, pp. 691–699.

[2]Glezer, A., Amitay, M., and Honohan, A. M., "Aspects of Low- and High-Frequency Aerodynamic Flow Control," No. 2003-0503 in AIAA Paper, 2003.

[3]Mittal, R., Kotapati, R. B., and Cattafesta, L. N., "Numerical Study of Resonant Interactions and Flow Control in a Canonical Separated Flow," No. 2005-1261 in AIAA Paper, 2005.

[4]Mittal, R. and Kotapati, R., "Resonant mode interaction in a canonical separated flow," *Proc. The Sixth IUTAM Symposium on Laminar-Turbulent Transition, Bangalore, India, December 13-17*, edited by R. Govindarajan, Springer, 2004.

[5]Roshko, A., "On the development of turbulent wakes from vortex streets," Tech. Rep. 1191, NACA, 1954.

[6]Ho, C.-M. and Huerre, P., "Perturbed Free Shear Layers," *Annu. Rev. Fluid Mech.*, Vol. 16, 1984, pp. 365–424.

[7]Seifert, A., Bachar, T., Koss, D., Shepshelovich, M., and Wygnanski, I., "Oscillatory Blowing: A Tool to Delay Boundary Layer Separation," *AIAA J.*, Vol. 31, 1993, pp. 2052–2060.

[8]Seifert, A. and Pack, L., "Oscillatory Control of Separation at High Reynolds Numbers," *AIAA J.*, Vol. 37, 1999, pp. 1062–1071.

[9]Glezer, A. and Amitay, M., "Synthetic Jets," *Annu. Rev. Fluid Mech.*, Vol. 34, 2002, pp. 503–532.

[10]Mittal, R. and Rampunggoon, P., "On the Virtual Aero-Shaping Effect of Synthetic Jets," *Phys. Fluids*, Vol. 14, 2002, pp. 1533–1536.

[11]Seifert, A. and Pack, L., "Separation Control at Flight Reynolds Numbers – Lessons Learned and Future Directions," No. 2000-2542 in AIAA Paper, 2000.

[12]Greenblatt, D. and Wygnanski, I., "Effect of Leading-Edge Curvature on Airfoil Separation Control," *J. Aircraft.*, Vol. 40, 2003, pp. 473–481.

[13]Pack, L., Schaeffler, N., Yao, C., and Seifert, A., "Active Control of Flow Separation from the Slat Shoulder of a Supercritical Airfoil," No. 2002-3156 in AIAA Paper, 2002.

[14]Na, Y. and Moin, P., "Direct Numerical Simulation of a Separated Turbulent Boundary Layer," *J. Fluid Mech.*, Vol. 370, 1998, pp. 175–201.

[15]Ye, T., Mittal, R., Udaykumar, H. S., and Shyy, W., "An Accurate Cartesian Grid Method for Viscous Incompressible Flows with Complex Immersed Boundaries," *J. Comp. Phys.*, Vol. 156, 1999, pp. 209–240.

[16]Bozkurttas, M., Dong, H., Sheshadri, V., Mittal, R., and Najjar, F., "Towards Numerical Simulation of Flaping Foils on Fixed Cartesian Grids," No. 2005-0079 in AIAA Paper, 2005.

[17]Najjar, F. M. and Mittal, R., "Simulations of Complex Flows and Fluid-Structue Interaction Problems on Fixed Cartesian Grids," *Proc. FEDSM'03,* 4^{th} *ASME-JSME Joint Fluids Engineering Conferece, Honolulu, Hawaii*, FEDSM2003-45577, 2003, pp. 184–196.